A Ground-Motion Prediction Model for Shallow Crustal Earthquakes in Greece

David M. Boore[*1], Jonathan P. Stewart[2], Andreas A. Skarlatoudis[3], Emel Seyhan[4], Basil Margaris[5], Nikos Theodoulidis[5], Emmanuel Scordilis[6], Ioannis Kalogeras[7], Nikolaos Klimis[8], and Nikolaos S. Melis[7]

─────── **ABSTRACT** ───────

Using a recently completed database of uniformly processed strong-motion data recorded in Greece, we derive a ground-motion prediction model (GMPM) for horizontal-component peak ground velocity, peak ground acceleration, and 5% damped pseudoacceleration response spectra, at 105 periods ranging from 0.01 to 10 s. The equations were developed by modifying a global GMPM, to account for more rapid attenuation and weaker magnitude scaling in the Greek ground motions than in the global GMPM. Our GMPM is calibrated using the Greek data for distances up to 300 km, magnitudes from 4.0 to 7.0, and time-averaged 30 m shear-wave velocities from 150 to 1200 m/s. The GMPM has important attributes for hazard applications including magnitude scaling that extends the range of applicability to M 8.0 and nonlinear site response. These features are possible because they are well constrained by data in the global GMPM from which our model is derived. An interesting feature of the Greek data, also observed previously in studies of mid-magnitude events (6.1–6.5) in Italy, is that they are substantially overpredicted by the global GMPM, which may be a repeatable regional feature, but may also be influenced by soil–structure interaction. This bias is an important source of epistemic uncertainty that should be considered in hazard analysis.

KEY POINTS

- The article develops a ground-motion prediction model for Greece, using a recently compiled database.
- The model is a modification of a global hazard model, but we find weaker ground motions than in global models.
- The model will be useful for hazard calculations to **M** = 8.0 in Greece, including nonlinear effects.

Supplemental Material

INTRODUCTION

As described in B. Margaris *et al.* (unpublished manuscript, 2021, see Data and Resources)—a companion paper to this article—the network of digital strong-motion instruments in Greece has increased substantially, since 2000, and these instruments have provided data from numerous well-recorded events. Moreover, the metadata describing the source, path, and site characteristics for new and older recordings, such as magnitude, distance, and V_{S30}, have been substantially improved as part of a long-term effort to raise the level of data quality and modeling in Greece to levels typically applied in Next Generation Attenuation (NGA) projects, such as NGA-West2 for active tectonic regions (Bozorgnia *et al.*, 2014).

In this article, we use these data to derive a ground-motion prediction model (GMPM) for shallow (focal depth ≤30 km)

crustal earthquakes in Greece. Our objective is for the model to be suitable for the conditions that control seismic hazard at the long return periods used in engineering design; disaggregation indicates these conditions to typically involve events with magnitudes in the range of 6.5–7.0 and distances less than 20 km. Such conditions are challenging for model development for two main reasons: (1) the upper portion of the magnitude range is near the limit of empirical datasets for Greece (B. Margaris *et al.*, unpublished manuscript, 2021, see Data and Resources) and Europe (Akkar, Sandıkkaya, Şenyurt, *et al.*, 2014; Bindi *et al.*, 2019; Lanzano *et al.*, 2019); and (2) the strong shaking that occurs under these conditions produces nonlinear site response for soil sites, which may be difficult to evaluate directly from data due to limited observations. As a result of these and other factors, the models are often used

in practice for ranges of conditions that may be poorly represented in empirical datasets.

To overcome these difficulties, our model development process modifies the Boore *et al.* (2014) global GMPM for application in Greece. The Boore *et al.* (2014) model applies for intensity measures from earthquakes in active crustal regions, and it is reasonably well constrained for the aforementioned hazard-controlling conditions. The modifications are targeted toward model attributes that are known to be regionally variable, including the constant term, anelastic attenuation, and site response. Similar approaches have been used previously for Italy, New Zealand, and Turkey (Scasserra *et al.*, 2009; Bradley, 2013; Gülerce *et al.*, 2016). Our approach differs from those used to develop the most currently available models, including models intended specifically for Greece (Danciu and Tselentis, 2007; Chousianitis *et al.*, 2018) and others intended for Europe (Akkar, Sandıkkaya, and Bommer, 2014; Bindi *et al.*, 2014; Kotha *et al.*, 2016, 2020; Kuehn and Scherbaum, 2016). Those Greece and Europe models are derived independently from other GMPMs, using datasets restricted to those regions.

Because the model developed here is Greece-specific, we briefly review prior Greece-specific models. The most recent previous equations for pseudospectral acceleration (PSA; Danciu and Tselentis, 2007) only used analog data recorded before 2000; the equations were restricted to distances less than 136 km, the site conditions were parameterized by a few site classes, and the equations were given for periods up to 4.0 s. A more recent study (Chousianitis *et al.*, 2018) used some data after 1999, but equations were not provided for PSA. They provide equations for peak ground acceleration (PGA) and peak ground velocity (PGV), for distances up to 200 km and a site parameterization similar to Danciu and Tselentis (2007). The equations of both Danciu and Tselentis (2007) and Chousianitis *et al.* (2018) have a linear magnitude dependence, whereas the most recent GMPMs find a nonlinear dependence, including those in this article, with the scaling of ground motion being stronger for small magnitudes than large magnitudes for a fixed distance.

The GMPM proposed here for Greece is developed for the following horizontal-component ground-motion intensity measures (GMIMs): pseudoacceleration 5% damped response spectra (PSA) at 105 periods ranging from 0.01 to 10 s, PGA, and PGV. The range of applicable moment magnitudes directly constrained by data is 4.0–7.0, but given the "borrowing" of magnitude scaling from a global model, the GMPM can be applied (with additional uncertainty) up to $\mathbf{M}$ 8.0 events. The distance range is 0–300 km, and the range of applicable site conditions (based on time-averaged 30 m shear-wave velocity, V_{S30}) is 150–1200 m/s.

Following this introduction, we first discuss the data used in the analysis. We then provide the set of equations that define our GMPM, and the derivation of the coefficients in those equations is given next (the coefficients are provided in the supplemental material to this article). This is followed by some comparisons of GMIMs from our GMPM with those from Boore *et al.* (2014; hereafter, BSSA14), and previously published GMPMs that are specifically for Greece. The article concludes with the Summary and Discussion section.

DATA

The development of the database used in this article is described in B. Margaris *et al.* (unpublished manuscript, 2021, see Data and Resources). The data are from horizontal-component recordings, converted to RotD50 (Boore, 2010), for shallow crustal earthquakes. We used a subset of the dataset for which focal depths are less than or equal to 30 km, and the maximum source-to-site distance does not exceed 300 km. Based on the location of the subducting plate, a maximum depth of 50 km was used in B. Margaris *et al.* (unpublished manuscript, 2021, see Data and Resources) to largely avoid including subduction earthquakes in the database. Our maximum depth of 30 km was chosen to make it even less likely that intermediate depth in-slab events, which are the most common subduction events, are included in our analysis. To avoid using singly recorded events and to include data at distances of most engineering interest, we impose the requirement that recordings are used only for events with at least two recordings within 80 km (in BSSA14, the greater amount of data allowed this requirement to be events with at least four recordings within 80 km). Trials with several other criteria gave results similar to those in this article.

PSAs for a particular recording were not used for periods greater than the maximum usable period ($T_{highest}$) for that record, as given in the flatfile provided in B. Margaris *et al.* (unpublished manuscript, 2021, see Data and Resources). We assume that PGV corresponds to a period of 0.5 s for the purpose of this data selection step, following Bommer and Alarcon (2006, see also Booth, 2007) and based on plots of PGV and PSA for various periods versus distance and magnitude. After looking at between-earthquake and within-earthquake residuals, we identified 44 records that we considered to be outliers. About 37 of these are from a single earthquake with $\mathbf{M} = 5.8$ and reverse-slip mechanism (Eqk_ID = 1697). When included in the analysis, the between-earthquake residuals for this event were negative, with absolute values between 2.5 and 3.5 times the between-event variability in our model (0.41 for $\mathbf{M} = 5.8$) for all GMIMs. We checked the magnitude and found it to be correct, and at this time we do not know the reason for the strongly negative between-event residuals. Removing the 44 records from the dataset used in the analysis does not change the results in any appreciable way. The supplemental material includes files showing which records were used in the analysis, so that others can repeat our analysis if desired. Finally, we imposed a magnitude–distance-instrument-type screening, similar to that used in BSSA14, but with a modification for modern digital instruments to deal with residuals of smaller earthquakes increasing with
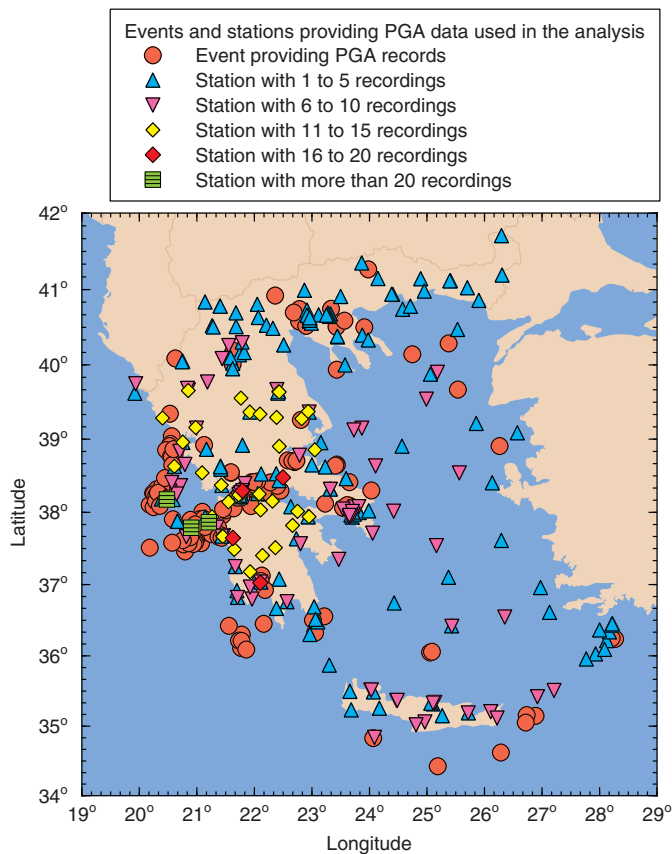
Figure 1. Map of Greece showing locations of events and stations in the B. Margaris *et al.* (unpublished manuscript, 2021, see Data and Resources) database that have produced recordings that meet the screening criteria applied in this article. Stations are sorted by the number of recordings per site, ranging from 1 to >20. The color version of this figure is available only in the electronic edition.

distance beyond about 200 km. We assume that these trends are due to the well-known effect on the distance decay if small amplitudes are below the noise levels for recordings at large distances.

Figure 1 shows the distribution of events and stations from the B. Margaris *et al.* (unpublished manuscript, 2021, see Data and Resources) dataset after the earlier screening is applied; the stations are sorted by the number of recordings per site. The stations apparently in the sea are on small islands that do not appear in the figure.

The magnitude and distance measures used in the analysis are moment magnitude, **M**, and Joyner–Boore distance, R_{JB} (the closest horizontal distance from a site to the vertical projection of the fault rupture surface onto the Earth's surface). Not all events in the flatfile have had finite-fault solutions derived for them; these are typically smaller magnitude events. For such events, B. Margaris *et al.* (unpublished manuscript, 2021, see Data and Resources) applied the simulation procedure of Contreras *et al.* (2020), a refined version of the

procedure originally developed by Chiou and Youngs (2008), to derive distance parameters that account for fault dimension (including rupture distance, R_{RUP}, and R_{JB}).

The magnitude–distance distribution of the data used in this article are shown in Figure 2, for periods of 0.1 and 10 s (in this article, for brevity we often use a phrase such as "a period of 0.1 s" to mean "a pseudoresponse spectrum GMIM for a period of 0.1 s"). As a result of most recordings being on high-resolution digital recorders, there is a much more uniform distribution of recordings in magnitude and distance space than in previous studies of Greek data (e.g., Danciu and Tselentis, 2007). Figure 2 contains data using the BSSA14 magnitude–distance-instrument type screening, but only data to the left of the revised screening shown in the figure were used for the final GMPM produced in this article. Comparing this figure with a similar one in BSSA14 (their fig. 2), we see some important differences that are part of our motivation to base our GMPM on residuals of the data, with respect to prediction from the BSSA14 GMPM: BSSA14 had more data at close distances, as well as for magnitudes less than 5.0 and greater than about 6.5. These differences in the magnitude–distance distribution are particularly acute at long periods, as there are few data for periods of 5 s or greater in our dataset (as shown in Fig. 2 for 10 s period). Figure 2 also shows that there are few recordings in our dataset for small magnitudes at a period of 10 s. This reduction is particularly noticeable for magnitudes less than 4.8, and the reduction occurs abruptly between periods of 4.6 and 4.8 s. This is a result of the $T_{highest}$ data selection criteria used in our analysis.

The number of events and records used in our final analysis are shown in Figure 3, as a function of period (for all magnitudes). The decrease in the number of records and events at long periods is the result of low-cut filtering used in the data analysis and application of the consequent $T_{highest}$ (a fraction of the inverse of the filter frequency) in the data selection. The number of strike-slip faulting events and records from such events is also greater than for normal-slip events, and both are greater than for reverse-slip events. The relative number of strike-slip and normal-slip events is opposite to that shown in a figure in B. Margaris *et al.* (unpublished manuscript, 2021, see Data and Resources) (their fig. 8), because singly recorded earthquakes have been eliminated from our dataset.

To see the basic distance and magnitude scaling characteristics of the data, response spectra from strike-slip earthquakes, adjusted to $V_{S30} = 760$ m/s using the Seyhan and Stewart (2014) site amplification model, are plotted against distance for four periods in Figure 4. The graphs clearly show curvature of the attenuation of motion with distance, with the rate of distance attenuation at large distance ($R_{JB} > 80$ km) being greater for short periods than for long periods. Curvature in the distance attenuation function is accommodated by including an anelastic term in the path function, as described in The GMPM section. There is also a suggestion of distance
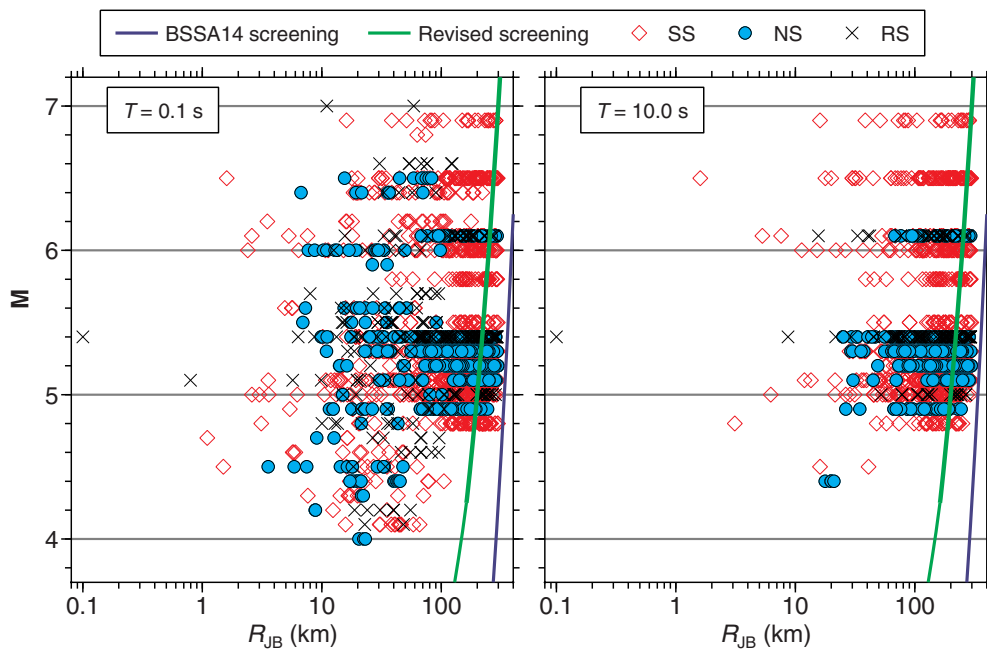
Figure 2. Moment magnitude–distance distribution of recordings used in this article, separated by fault mechanism (*SS*, *NS*, and *RS* are strike-slip, normal-slip, and reverse-slip events, respectively). The two graphs are for different response spectral periods (0.1 and 10.0 s). The lines show the magnitude–distance cutoffs for recordings from modern digital instruments, both as used in Boore *et al.* (2014; hereafter BSSA14) and the revised cutoffs for this article. The data shown used the revised BSSA14 cutoff criteria, but only data to the left of the revised screening criteria were used in the analysis in this article. The color version of this figure is available only in the electronic edition.
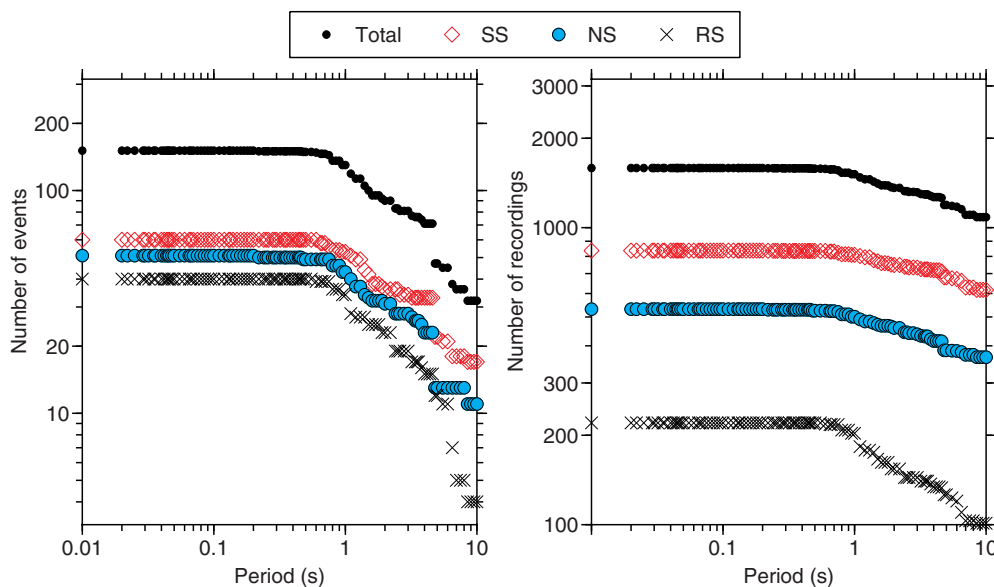

Figure 3. The number of events (left graph) and recordings (right graph) used in the analysis, as a function of period, for the different fault mechanisms. Plots for peak ground acceleration (PGA) and peak ground velocity (PGV) are not shown, as their numbers are very close to those for periods of 0.01 and 0.5 s, respectively. The color version of this figure is available only in the electronic edition.

saturation of motions at short distance (i.e., the motions for a particular magnitude trend toward a constant value at small distances). The graphs show an increase of magnitude scaling with period for a fixed distance. Similar graphs in BSSA14, with more data, agree with what is shown in Figure 4, but those graphs also show the need for nonlinear magnitude scaling for a fixed distance and period, as well as magnitude-dependent differences in attenuation. Because of the smaller number of recordings, however, the need for the nonlinear magnitude scaling and the magnitude dependent distance is not as obvious in Figure 4. This is another reason to rely on the BSSA14 GMPM, adjusting those coefficients for which there are adequate data from Greece to determine the adjustment, while retaining the other BSSA14 coefficients.

THE GMPM

The GMPM is composed of a set of ground-motion prediction equations (GMPEs). The GMPEs are very similar to those in BSSA14, with some exceptions: there is no basin depth term (lacking such data for Greece) or regional adjustments (in view of the limitations of the dataset, we consider all of Greece to be one region), the site response is constant for V_{S30} less than a specified value, and the equation for ϕ (the within-event aleatory variability) is not a function of $\mathbf{M}$, R_{JB}, and V_{S30}. The predicted GMIMs (Y) are given by

$$\ln Y = F_E(\mathbf{M}, mech) + F_P(R_{JB}, \mathbf{M})$$
$$+ F_S(V_{S30}, R_{JB}, \mathbf{M}, mech)$$
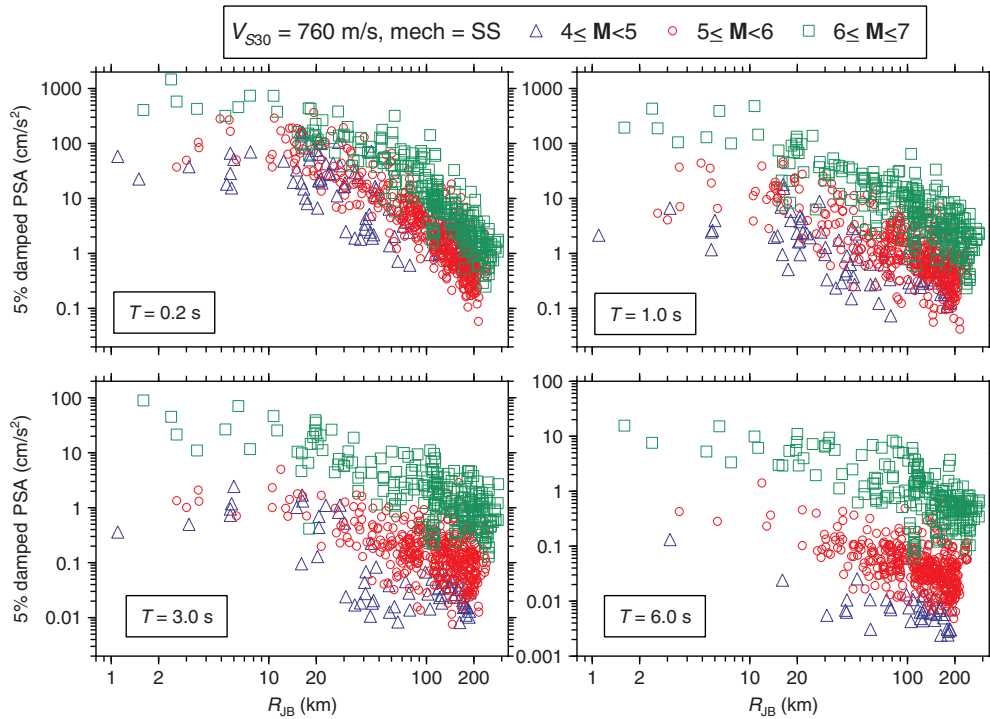$$+ \varepsilon_n \sigma(\mathbf{M}), \qquad (1)$$

Figure 4. Response spectral values used in this article, plotted against distance for four periods and separated into three magnitude ranges. Only data from strike-slip events are shown, and the values have been adjusted to $V_{S30} = 760$ m/s. The color version of this figure is available only in the electronic edition.

in which "ln" is the natural logarithm, and F_E, F_P, and F_S are functions for the event ("E"), path ("P"), and site ("S") contributions to the motion. The standard normal variate ε_n is the fractional number of standard deviations σ of a predicted motion from the mean (e.g., $\varepsilon_n = 2.0$ will result in a predicted motion two standard deviations greater than the mean). Y has units of cm/s for PGV and cm/s² for PGA and PSA.

All terms in the equations later, except for the predictor variables ($\mathbf{M}$, R_{JB}, V_{S30}, and fault type [*mech*]), can be dependent on period; for simplicity of presentation, the variable for period has not been shown explicitly.

The equation for the event components of the GMPM is given by

$$F_E(\mathbf{M}, mech)$$
$$= \begin{cases} e_0 U + e_1 SS + e_2 NS + e_3 RS + e_4(\mathbf{M}-\mathbf{M}_h) + e_5(\mathbf{M}-\mathbf{M}_h)^2 & \mathbf{M} \leq \mathbf{M}_h \\ e_0 U + e_1 SS + e_2 NS + e_3 RS + e_6(\mathbf{M}-\mathbf{M}_h) & \mathbf{M} > \mathbf{M}_h \end{cases},$$
(2)

in which *mech* is shorthand for the fault-type predictor variables U, SS, NS, and RS, which have values of 1.0 for unspecified, strike-slip, normal-slip, and reverse-slip fault types, and 0.0 otherwise. $\mathbf{M}$ is the moment-magnitude predictor variable, and $\mathbf{M}_h$ is a period-independent hinge magnitude given in the table of coefficients. The basis for the specific value is discussed later, in the section describing revisions to the source model.

The path function is given by

$$F_P(R_{JB}, \mathbf{M}) = [c_1 + c_2(\mathbf{M}-\mathbf{M}_{ref})]$$
$$\ln(R/R_{ref}) + c_3(R-R_{ref}), \quad (3)$$

in which $\mathbf{M}_{ref}$ and R_{ref} are period-independent constants (chosen as 4.5 and 1.0 km, respectively), and the variable R is calculated as

$$R = \sqrt{R_{JB}^2 + h^2}, \quad (4)$$

in which R_{JB} is the predictor variable, in kilometers, defined previously, and h is a period-dependent finite-fault factor given in the table of coefficients included in the supplemental materials. The values for h come from BSSA14; we found no reason to modify them.

The site function is given by the addition of linear and nonlinear site-response functions:

$$F_S(V_{S30}, R_{JB}, \mathbf{M}, mech) = F_{lin} + F_{nl}. \quad (5)$$

The variable *mech* is included because the PGA in the nonlinear site response can depend on *mech*. The right side of the equation for $F_S(V_{S30}, R_{JB}, \mathbf{M}, mech)$ in BSSA14 used the combination $\ln(F_{lin}) + \ln(F_{nl})$ rather than $F_{lin} + F_{nl}$. $F_S(V_{S30}, R_{JB}, \mathbf{M}, mech)$ in BSSA14 and here is the same, but the meaning of F_{lin} and F_{nl} in the BSSA14 equation for F_S is different than in this article. We made this change in keeping with the meaning of the other "F" functions in the equations for the GMPM. The right side of equation (5) is also the same as equation (1) in Stewart *et al.* (2020).

The linear site response is given by

$$F_{lin} = \begin{cases} c_{lin} \ln(V_1/V_{ref}) & V_{S30} \leq V_1 \\ c_{lin} \ln(V_{S30}/V_{ref}) & V_1 < V_{S30} \leq V_c \\ c_{lin} \ln(V_c/V_{ref}) & V_c < V_{S30} \end{cases}. \quad (6)$$

This differs from BSSA14 in that the amplification is constant for $V_{S30} \leq V_1$, as in Stewart *et al.* (2020). The predictor variable is V_{S30}, with units of m/s and V_{ref} is period independent, chosen as 760 m/s. V_1 and V_c were determined from the analysis in this article and in BSSA14. All variables and coefficients, other than the predictor variable V_{S30}, are provided in the table of coefficients.

The nonlinear site response is given by

$$F_{nl} = f_1 + f_2 \ln(1 + PGA_r/f_3), \qquad (7)$$

in which PGA_r is the PGA for a reference rock site (in cm/s^2), obtained by evaluating equation (1) with predictor variables R_{JB}, **M**, *mech*, and $V_{S30} = 760$ m/s. f_2 is given by the following equation (originally from Chiou and Youngs, 2008):

$$f_2 = f_4 [\exp\{f_5(\min(V_{S30}, 760) - 360)\} - \exp\{f_5(760 - 360)\}], \qquad (8)$$

and f_1, f_3, f_4, and f_5 are given in the coefficient table.

The aleatory variability σ is a combination of the within-event variability ϕ and the between-event variability τ, as follows:

$$\sigma(\mathbf{M}) = \sqrt{\phi^2 + \tau(\mathbf{M})^2}, \qquad (9)$$

in which the period-dependent ϕ is given in the coefficient table, and the **M**-dependent between-event aleatory variability is given by

$$\tau(\mathbf{M}) = \begin{cases} \tau_1 & \mathbf{M} \leq \mathbf{M}_{\tau 1} \\ \tau_1 + (\tau_2 - \tau_1)\frac{\mathbf{M} - \mathbf{M}_{\tau 1}}{\mathbf{M}_{\tau 2} - \mathbf{M}_{\tau 1}} & \mathbf{M}_{\tau 1} < \mathbf{M} < \mathbf{M}_{\tau 2}, \\ \tau_2 & \mathbf{M} \geq \mathbf{M}_{\tau 2} \end{cases} \qquad (10)$$

in which τ_1, τ_2, $\mathbf{M}_{\tau 1}$, and $\mathbf{M}_{\tau 2}$ are given in the coefficient table. The equation for τ is the same as in BSSA14, except that $\mathbf{M}_{\tau 1}$, and $\mathbf{M}_{\tau 2}$ have different values in our GMPM. ϕ, in our study, is not dependent on **M**, R_{JB}, and V_{S30}, as it is in BSSA14. The explanation for the form of the aleatory variability functions is given later.

MODEL DEVELOPMENT

The amount and quality of data from Greece, as given in the B. Margaris *et al.* (unpublished manuscript, 2021, see Data and Resources) database, is sufficient to derive GMPEs that would describe ground-motion features across the range of the data. However, as described in the Introduction, we adopt a different approach motivated by our objective of developing models that are effective for hazard-controlling conditions. Accordingly, we looked at the residuals of the Greek data relative to a global GMPM derived from a richer dataset and derived adjustments for a few of the coefficients required to fit the Greek data. We used the adjusted coefficients, as well as coefficients that needed no adjustments, for the GMPM that is the product of the work in this article.

Method

The essence of the method is to compute total residuals of the data relative to predictions from the BSSA14 global model, perform mixed-effects analysis of the residuals to separate the total

residuals into between-event and within-event components, look for trends of the between-event and within-event residuals with various predictor variables, revise the relevant GMPE coefficients to remove or reduce the trends (usually by doing a regression of the relevant residuals against predictor variables, finding an adjustment factor, and then adding this factor to the original coefficient), and then repeat the earlier steps one or more times. The final step in the analysis is to smooth the coefficients to be used in the new GMPEs. Examples of this process for other datasets are given in Scasserra *et al.* (2009), Skarlatoudis (2017), and Boore (2020). The total residual is defined by

$$\mathcal{R}_{ij} = \ln(Y_{ij}) - \mu_{\ln Y}(\mathbf{M}^i, R_{JB}^{ij}, V_{S30}^j, mech^i), \qquad (11)$$

in which i and j designate an event and a site, respectively, $\ln(Y_{ij})$ is a measured GMIM, and $\mu_{\ln Y}$ is the mean natural log GMIM from a reference GMPM. The i and j indexes are shown as superscripts in the right-most term in equation (11), to avoid notational complexity with the two predictor variables that have subscripts.

The total residuals are fit, period by period, to the following equation using mixed-effects analysis (R Core Team 2019, see Data and Resources):

$$\mathcal{R}_{ij} = B + \eta_i + \varepsilon_{ij}, \qquad (12)$$

in which B is the overall bias, and η_i and ε_{ij} are between-event (also known as "event terms") and within-event residuals. Those residuals have zero mean and standard deviations denoted by τ and ϕ.

The mixed-effects analysis, described earlier, was repeated for PGV, PGA, and 105 response spectral periods between 0.01 and 10 s. For each analysis, graphs were prepared of the between-event residuals against **M**, *mech*, and hypocentral depth (Z_{hyp}), and of the within-event residuals against R_{JB} and V_{S30}. An example is shown in Figure 5, for a period of 0.2 s (chosen because it had some of the most pronounced trends of the residuals with the predictor variables). The BSSA14 GMPM, with no modifications to the original coefficients, was used to compute the total residual for the analysis. From this figure and others like it, we found that modifications of some of the BSSA14 coefficients were needed. These are discussed in separate sections later.

Before giving the details about the modified coefficients, we discuss here the smoothing done to obtain the final coefficients for the GMPEs. The smoothing was a combination of averaging the coefficients for 11 periods centered on a given period and subjective smoothing guided by the variation of the BSSA14 coefficients with period, which are more robustly determined than the adjusted coefficients in our analysis, at least for longer periods. The subjective smoothing was done when the adjustments to the BSSA14 coefficients had
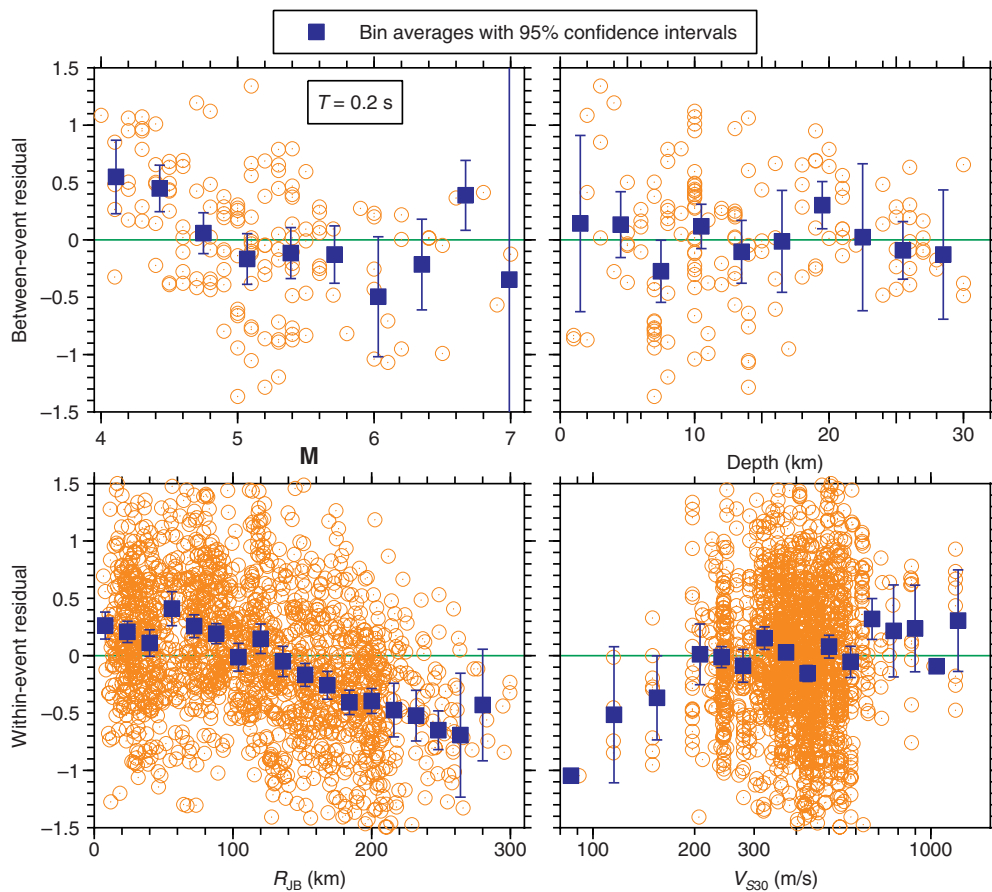
Figure 5. Between-event and within-event residuals (open circles) from the mixed-effects analysis, plotted against key metadata, for a period of 0.2 s. The predicted values used to compute the total residuals (equation 11) came from the BSSA14 ground-motion prediction model (GMPM) without modification, and no region adjustment was made to the anelastic coefficient c_3. Solid squares are averages in metadata bins. The color version of this figure is available only in the electronic edition.

We repeated the residual analysis to make sure that no unusual trends were introduced by using the smoothed coefficients.

Revisions to path model

The first and most important modification to the BSSA14 GMPM was in the path function. The need for this modification is shown by the strong trend in the graph of within-event residuals versus R_{JB} in Figure 5, where the negative trend of the residuals indicates that the data attenuate more rapidly with distance than the predicted values. We made similar graphs using log and linear scales for the distance axis, and determined that a simple and sufficient modification to the BSSA14 path equation was to find an adjustment for the anelastic coefficient c_3 (which can remove a linear trend in residuals plotted against a linear distance axis). The geometric spreading model was not modified.

We developed the adjustment by fitting the within-event residuals with a linear function of R_{JB} period-by-period and adding the slope of that function to the BSSA14 c_3. The result is shown in Figure 6. The BSSA14 global and Region 3 anelastic coefficients are also shown in that figure (Region 3 is for Italy and Japan; these regions had the most rapid attenuation among the various regions considered in BSSA14). The adjusted c_3 coefficient is generally more negative than the BSSA14 global or Region 3 coefficients, indicating more rapid attenuation of the ground motions in Greece than for either the global database used in BSSA14 or the Italy and Japan region. On the other hand, the c_3 values regressed from the data for Greece become positive for longer periods (as does the coefficient for Region 3 in BSSA14). The BSSA14 global c_3 coefficient was constrained to be less than or equal to 0.0, even though the analysis that led to that coefficient showed positive values for most of the magnitude bins used in determining the coefficient (fig. 4.3 in Boore *et al.*, 2013). We have not applied this constraint in the present model. Although negative anelastic attenuation seems unphysical, it may reflect phenomena, such as dominance of longer-period surface waves at large

noticeable variations over small ranges of periods, probably because of relatively small numbers of data used to obtain the adjustments. In this article we show the smoothed coefficients.
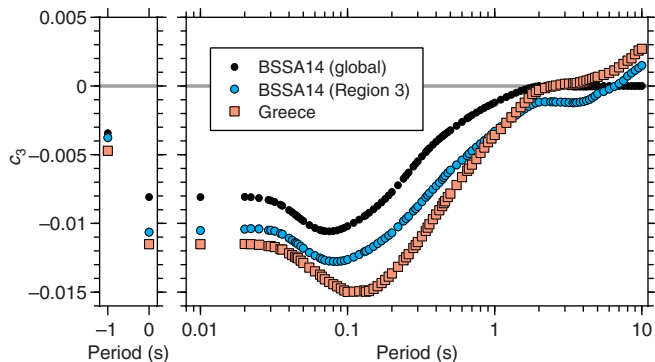

Figure 6. The smoothed anelastic distance coefficient for Greece, as determined in this article and for BSSA14. Periods of −1 and 0 correspond to PGV and PGA, respectively. The color version of this figure is available only in the electronic edition.

distances, that are not included in the geometric spreading model. The impact of this model feature becomes significant only for distances beyond about 300–600 km, which is not of practical importance for most hazard and risk applications.

The physical reason for the more rapid attenuation, particularly for the shorter period motions, is not clear. One possibility mentioned by a reviewer is that the attenuation is due to propagation through the low-velocity and highly attenuating region above the subducting slab. Based on the locations of events and stations shown in the map in Figure 1, however, as well as the location of the subducting slab shown in figure 2 in Boore *et al.* (2009) and figure 5 in Skarlatoudis *et al.* (2013), we conclude that the effect of propagation through the attenuating material above the subducting slab would be minimal or nondetectable in the residuals analyses. The events along and in the inner side of the subduction trench (mainly near Crete) probably have very few back-arc recordings. Recordings from these events could influence the observed attenuation, if their propagation paths crossed the volcanic arc, as they would have traveled an adequate distance within the low-velocity layer for the motions to be strongly attenuated (at high frequencies). The chances of this happening are very small, due to our choice of hypocentral depths being less than 30 km. Because similar fast-attenuation effects have been observed in recent Italian events (e.g., Zimmaro *et al.*, 2018), this may be a feature that is relatively broadly encountered in the Mediterranean region.

A mixed-effects analysis using the BSSA14 model with the adjusted c_3 coefficient was performed. No trends of within-event residuals versus R_{JB} were found for residuals grouped into several magnitude bins (plots of the residuals are given in the supplemental material to this article). This analysis was done to determine if changes were needed to the BSSA14 geometrical spreading coefficients c_1 and c_2 (the latter of which expresses magnitude dependence). We saw no need to make changes.

Revisions to source model

Following adjustment of the path model, we next evaluated the need for potential revision of the BSSA14 source model, with an emphasis on the magnitude-scaling coefficient e_4 and the hinge magnitude $\mathbf{M}_h$ (we left e_5 and e_6 unchanged).

Revision of the magnitude-scaling model was primarily motivated by trends in the between-event residuals for small magnitudes, such as those seen in Figure 5 for $\mathbf{M}$ less than about 4.6. The results shown in Figure 5 for PSA at 0.2 s, and in similar figures for other periods, have a downward trend at small magnitudes (e.g., $\mathbf{M} < 4.6$ for 0.2 s), which suggests that the magnitude-scaling function should be flattened (by reducing parameter e_4). At larger magnitudes, trends are either flat or slightly upward (suggesting no change or steeper $\mathbf{M}$-scaling, respectively).

We experimented with a number of functions fit to the residuals and decided initially to use a bilinear function hinged
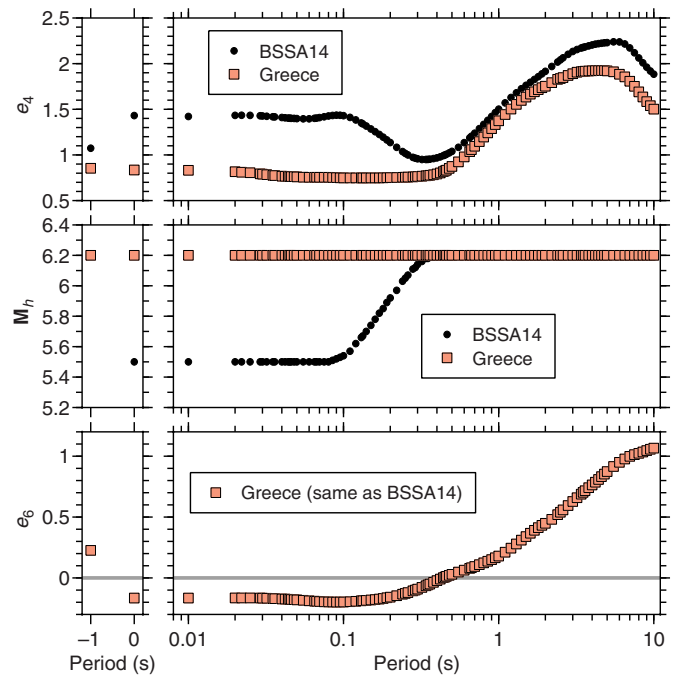

Figure 7. Smoothed magnitude-scaling coefficients for Greece, as determined in this article and for BSSA14 (the BSSA14 coefficient e_5 was used without change in the Greek GMPM). The e_6 coefficient from BSSA14 was not revised. The color version of this figure is available only in the electronic edition.

at the BSSA 14 $\mathbf{M}_h$; this function gave an adequate fit to the residuals and required the least change to the form of the F_E function. The slope of the bilinear function for $\mathbf{M} < \mathbf{M}_h$ was added to the BSSA14 coefficient, e_4. Figure 7 plots smoothed values of e_4, as well as the final values of e_6 and $\mathbf{M}_h$. For $\mathbf{M} > \mathbf{M}_h$, we considered two options. The first option was to add the slope from the bilinear function to e_6, which had the effect of increasing the GMIM with magnitude for $T < 1.5$ s, with no change to e_6 at longer periods. The second option was not to change e_6 from the BSSA14 coefficients, but to increase $\mathbf{M}_h$ modestly for short periods instead, which improved the fit for $\mathbf{M} > \mathbf{M}_h$. Although, both options produce similar model performance in terms of between-event residuals, we selected the second option, because the retention of the BSSA14 version of e_6 allows the large-magnitude scaling to be constrained from global data.

After redoing the mixed-effects analysis with a total residual computed using the BSSA14 GMPM with modified c_3, e_4, and $\mathbf{M}_h$ coefficients, we noticed a small nonzero mean of the between-event residuals for the various fault types, mainly for periods longer than about 3 s. As a result, we next modified the BSSA14 coefficients for fault type (e_0, e_1, e_2, and e_3) using the means as an adjustment factor to the BSSA14 coefficients and then smoothing the coefficients. The results are plotted in Figure 8a. As explained in BSSA14, the e_0 coefficient is derived as a weighted average of the other coefficients and is, therefore,

not shown in Figure 8 (there are too few data corresponding to a U fault type to determine e_0 from the regression analysis). For periods less than about 2 s, the coefficients for SS and RS faults are similar, and the NS coefficients are smaller than for SS and RS faults. This agrees with BSSA14 and the findings of Skarlatoudis *et al.* (2003) and Danciu and Tselentis (2007), using much more limited datasets. For longer periods, the RS coefficient becomes less than the SS and NS coefficients, but there are decreasing numbers of data in the various fault-type classes, as period increases. On the other hand, an approximation of the standard error of the mean (SEOM) of the smoothed coefficients (which are shown in Fig. 8) shows that the SS and NS coefficients are larger than the RS coefficients by more than one SEOM for periods greater than 3.6 s.

To complete this section on the source model, we show the magnitude scaling for various periods and fault types in Figure 9. This figure is based on a similar one in BSSA14, but in that figure the symbols represent data for each event adjusted to a reference distance using the path model, which was then used to fit the magnitude-scaling function shown in the figure. This is not the case in Figure 9, and, thus, care must be taken in interpreting the figure. The lines are from the revised function F_E. The symbols shown in Figure 9 are the result of adding the between-event residuals η_i from a mixed-effects analysis, using the revised coefficients to F_E evaluated at the appropriate magnitude to each between-event residual. The figure shows the variable magnitude scaling across GMIMs, as well as the relative differences due to fault type. The figure also shows the relatively limited data at longer periods and larger **M** (e.g., there are no RS data for $\mathbf{M} > \mathbf{M}_h$, for $T = 3$ and 10 s).

Model bias and revisions to constant terms

In the mixed-effects analysis using equation (12), the bias B is a fixed effect. The bias that is obtained after adjusting the path and source models, as described in the Revisions to Path Model and Revisions to Source Model sections, is shown, following some smoothing, in Figure 8b. The symbols labeled "Greece: $\mathbf{M} \geq 4.0$" is the bias in the coefficient file. It is a smoothed version of the bias obtained from a mixed-effects analysis of the Greek data for magnitudes greater than or equal to 4.0, when the Greek GMPM with no bias adjustment to the coefficients e_0, e_1, e_2, and e_3 is used to compute μ_{lnY} in equation (11). To investigate the sensitivity to the minimum magnitude, the unsmoothed bias for a minimum magnitude of 5.0 is also shown in Figure 8. The biases from the two minimum magnitudes are reasonably similar. This is not true, however, for the bias of the Greek data relative to the BSSA14 model (with the Region 3 anelastic attenuation) without modifications to the BSSA14 path and source functions. The large differences at short periods are a reflection of the need to adjust the short-period magnitude scaling in the BSSA14 GMPM for use in Greece, as discussed earlier. A striking feature of Figure 8 is that the biases for all cases are significantly smaller than 0.
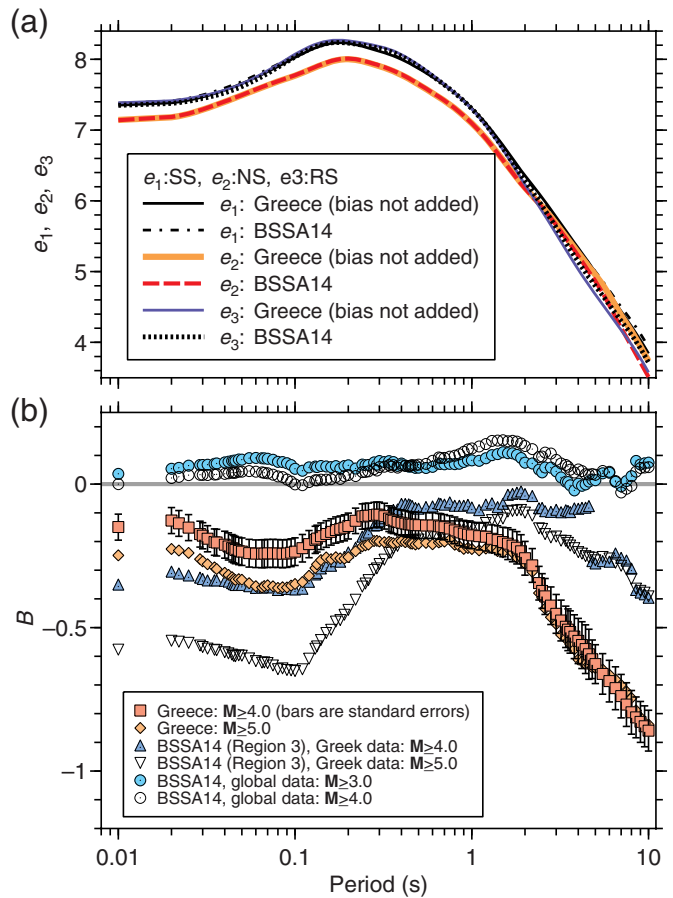

Figure 8. (a) The fault mechanism coefficients. The published coefficients for BSSA14 produce PGA and PSA with units of *g*; they have been converted for this figure to correspond to units of cm/s², which are the units used for the Greek GMPM. (b) The bias *B*, relative to predictions from either the BSSA14 GMPM or the Greek GMPM, as a function of period. Bias is shown for the proposed Greek GMPM and the BSSA14 model, when applied to Greek data (using Region 3 anelastic attenuation) and to the global data (where each recording's region was used in evaluating the GMPM). The bias was computed for several lower limits to the magnitudes used in the mixed-effects analysis, as indicated in the legend. The color version of this figure is available only in the electronic edition.

This indicates that the GMIMs from the recordings in Greece are smaller, on average, than those used in developing the BSSA14 GMPM. This finding of overprediction has been observed previously for individual earthquakes in Greece (B. Margaris *et al.*, unpublished manuscript, 2010, see Data and Resources) and Italy (Stewart *et al.*, 2012; Zimmaro *et al.*, 2018) (in the case of the pre-2014 publications, the bias was derived relative to the Boore and Atkinson, 2008, GMPM).

Figure 8 also shows the biases for the BSSA14 GMPM from two recent re-analyses of the NGA-West2 global dataset used to develop the BSSA14 GMPM. The biases are insensitive to the minimum magnitudes used in the analyses (3.0 and 4.0), and the biases are slightly positive and essentially flat. The non-zero values of the biases are caused by the BSSA14 constant
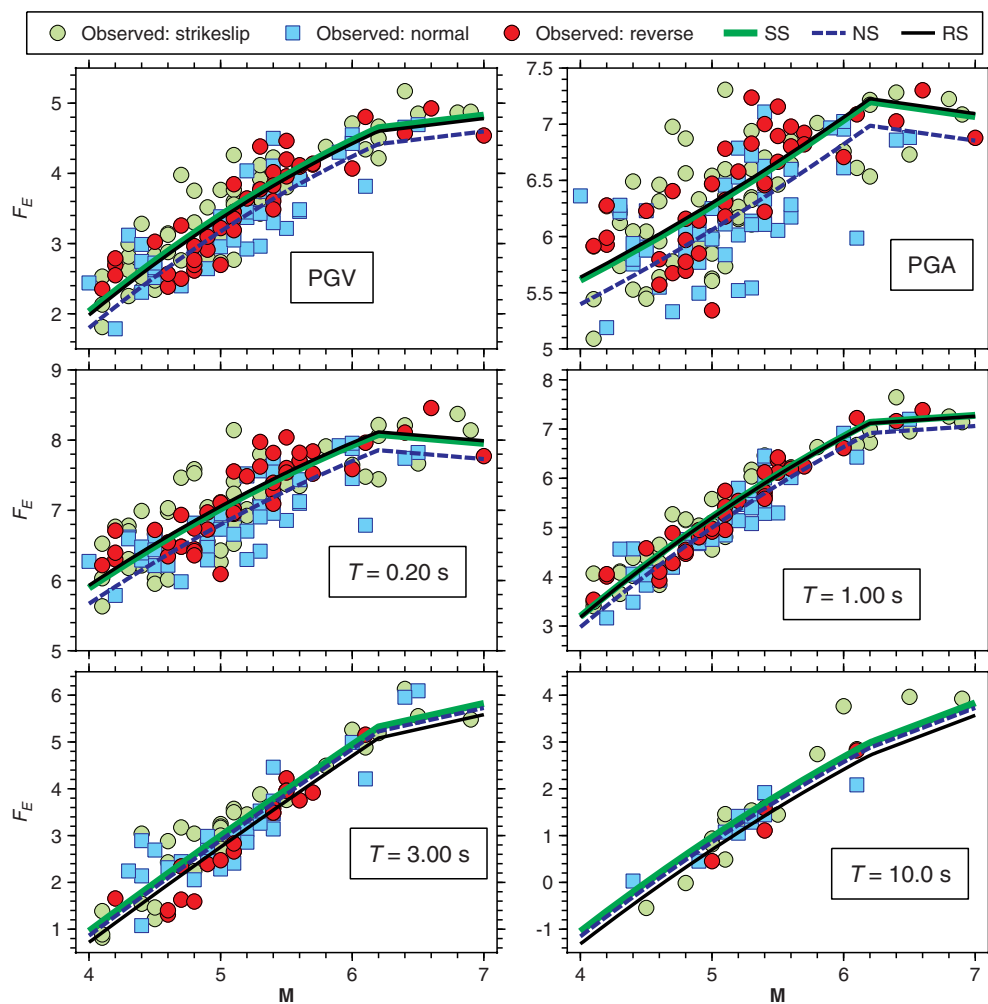
Figure 9. Magnitude scaling (F_E function) for the final Greek GMPM. The units of $\exp(F_E)$ are cm/s^2 for PGA and response spectra. Each symbol corresponds to a separate event. The symbols were computed by adding the between-event residuals for each event to the F_E, corresponding to the appropriate mechanism and magnitude for the event corresponding to each symbol. The bias B was added to the mechanism coefficients, but this will only affect the absolute values of F_E and not the relations between the symbols and F_E. The color version of this figure is available only in the electronic edition.

Greek instruments are placed in the basements or ground floors of buildings, and it has been shown that soil–structure interaction (SSI) reduces ground motions in basements relative to adjacent free-field sites (National Institute of Standards and Technology [NIST], 2012; Conti *et al.*, 2018; Sotiriadis *et al.*, 2019, 2020). SSI tends to reduce ground motions at short periods in a manner similar to that observed in Figure 8, but it has little impact at longer periods (typically >1 s). Although, SSI is a factor that could potentially influence the results, arguments against it being the sole (or dominant) source include:

- The bias decreases at longer periods after a stable region from about 0.3 to 2.0 s, which is not expected from SSI principles. (This decrease occurs well before the periods—generally greater than 4.6 s—where some of the coefficients in the iterative mixed-effects analysis show discontinuous changes with period, because of changing amounts of available data due to the use of T_{height} in selecting the data for our analysis.)

- Skarlatoudis (2017) found trends similar to those in Figure 8 in his analysis of Greek intraslab subduction GMIMs, as compared with global or Japan models. Many of the instruments used in that study were seismometers not housed in building structures (unlike the accelerometers used in the present study).

- The present findings are similar to previously observed trends from Italy, for which most of the instrument housings are relatively small structures.

Ultimately, we do not have a good explanation for the cause of the bias, but its persistence in recent literature suggests that it may be a regional feature, perhaps being due at short periods to unusually large attenuation in the upper few kilometers of the crust, as suggested by Hatzidimitriou *et al.* (1993), that should

and magnitude-scaling terms being set using a subset of the data with $R_{\text{JB}} < 80$ km, whereas the biases are evaluated using all data. The difference between the biases using the global dataset and the Greece dataset indicates a consistent difference between short-period ground motions in Greece relative to other regions globally. A similar bias may be present in Italy, as suggested by Stewart *et al.* (2012), Zimmaro *et al.* (2018), and results in Kotha *et al.* (2020; their fig. 11), but we have not formally investigated that as part of this study.

Although the Greek-data bias plotted in Figure 8 is a smoothed version of the bias from the mixed-effects analysis, little smoothing was required for periods less than about 4.7 s. The standard error of the means from the mixed-effects analysis were used with the smoothed coefficients, to show the uncertainty over most of the period range. Many of the
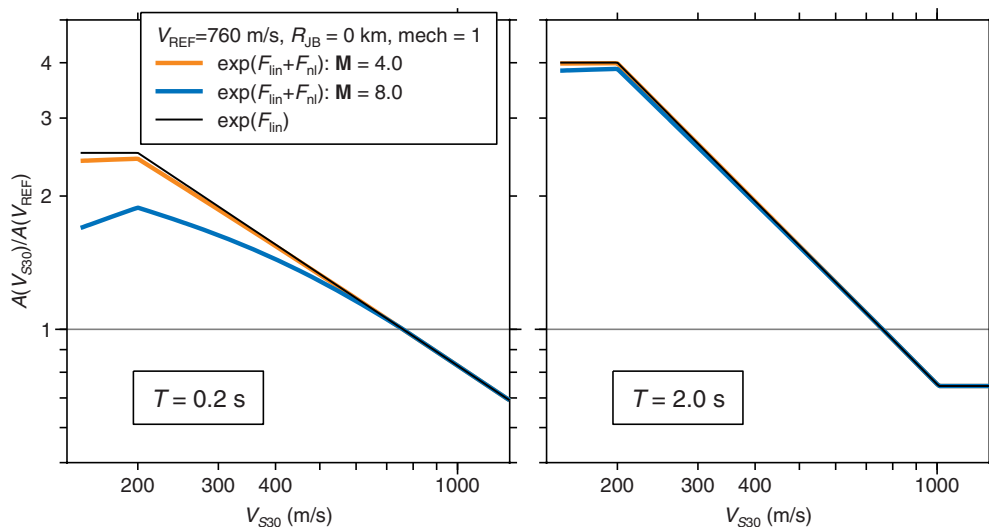
Figure 10. Site amplification for two specific cases and two periods. The linear, nonlinear, and total amplifications are shown. The two cases were chosen to highlight the difference in linear and nonlinear amplifications. The color version of this figure is available only in the electronic edition.

be included in the Greek GMPM. We provide the bias in the accompanying coefficient table (available in the supplemental material), but we do not add it to the fault-type coefficients e_0, e_1, e_2, and e_3 in that table. In application, if it is thought that the bias is due to SSI and GMIMs are to be predicted for free-field sites, it would be reasonable to use the e_0, e_1, e_2, and e_3 coefficients, as is in equation (2). On the other hand, if it is believed that SSI effects are not important and that the GMIMs in Greece are smaller as a result of repeatable regional effects, the bias B should be added to the fault-type coefficients before their use in equation (2). Of course, the observed bias could be a combination of regional and SSI effects, but without knowing the presumably period-dependent proportion of each, we make no attempt to separate the two contributions. In a later figure, we show GMIMs computed with and without the added bias.

Revisions to site amplification model

Based on Figure 5, an apparently needed change in the BSSA14 GMPM for applications in Greece is in the V_{S30} scaling at both large and, in particular, small values of V_{S30}. For $V_{S30} < 200$ m/s, there is a strong trend toward negative residuals with decreasing velocity. Although not shown here for brevity, this trend exists at all periods. For $V_{S30} > 600$ m/s, there is a tendency for the residuals to be positive, particularly, at periods between about 0.2 and 4 s. However, in the middle range of V_{S30} (approximately 200–600 m/s), corresponding to most of the data, the within-event residuals for all periods are well behaved, being close to 0.0.

The data at both ends of the V_{S30} range are from very few stations. For high V_{S30}, the highest value (1183 m/s) is from a single ITSAK station (VSK1). At the low end of the range (less

than 197 m/s), the data are from only three National Observatory of Athens stations (PREA, 115 m/s; KSLB, 137 m/s; and PATA, 150 m/s). Although we do not think that F_S should be adjusted to fit trends that might be driven by individual station amplifications, we have made a minor modification to the site amplification at the low end of the velocity range, using a functional form applied previously for stable continental regions (Stewart *et al.*, 2020). The modification is to make the amplification constant for $V_{S30} \leq V_1$, in which we have chosen $V_1 = 200$ m/s, based on the within-event residual plots. This modification has very little impact on the within-event residuals and is only noticeable at longer periods. Because the single ITSAK station with $V_1 = 1183$ m/s largely controls the trend at higher values of V_{S30}, we decided not to make any changes to F_S for $V_1 > 200$ m/s. For higher velocities, we assume, based on the residuals, that the V_{S30}-scaling parameter, c_{lin}, from BSSA14 is applicable to Greece.

The site amplifications from the model are illustrated in Figure 10 for two magnitudes (4.0 and 8.0), a single distance ($R_{JB} = 0$ km), a strike-slip mechanism (*mech* = 1), and two oscillator periods (0.2 and 2.0 s). The model parameters were chosen to illustrate the differences in linear and nonlinear site amplifications.

Aleatory variability model

The aleatory variability model describes between-event and within-event variability of GMIMs. A comparison of the within-event variability ϕ from the mixed-effects analysis and from BSSA14 is shown in Figure 11. Because the BSSA14 ϕ is a function of **M**, R_{JB}, and V_{S30}, we show the results for representative values of those predictor variables. The ϕ from the mixed-effects analysis, using the Greek GMPM coefficients in the table accompanying this article, is shown for two runs, with differing minimum magnitudes (4.0 and 5.0). As is clear from Figure 11, there is little dependence of ϕ for the Greek GMPM on the minimum magnitude. We have chosen to let the ϕ for our proposed GMPM depend only on period, as we do not feel there were enough data to support a model conditioned on additional predictor variables. We modified the ϕ from mixed-effects analysis to be nearly constant for periods longer than about 4.7 s, as we are less certain about our results for periods greater than this value and also felt that ϕ should
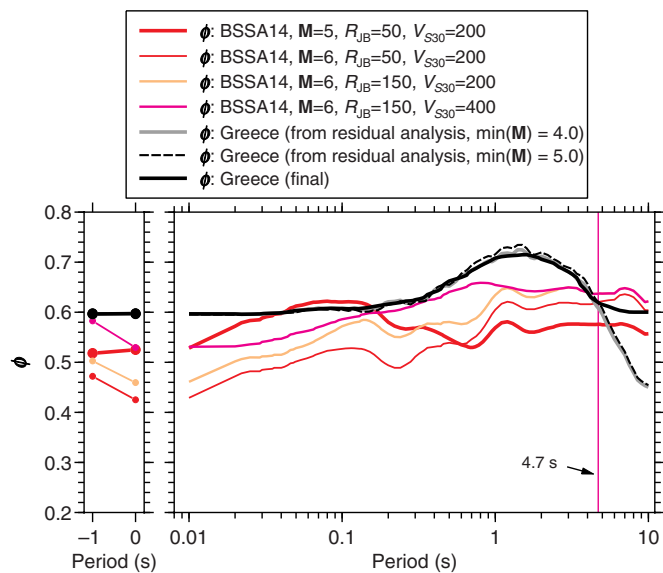
Figure 11. The within-event aleatory variability as a function of period. The color version of this figure is available only in the electronic edition.

Figure 12. The between-event aleatory variability as a function of magnitude. The individual τ values are standard deviations of the between-event residuals in magnitude bins. The purpose of this figure is to provide guidance for the choice of a magnitude-dependent τ. The individual symbols suggest a function given by the thin line, whereas the function adopted in this article is given by the thicker line (the reasons for the choice are given in the Aleatory Variability Model section). The color version of this figure is available only in the electronic edition.

not decrease with period over this range of periods. This modification of ϕ was guided by the BSSA14 results.

To explore the extension of the ergodic model for the within-event variability in this article to partially or fully non-ergodic models (Al Atik *et al.*, 2010), we performed a mixed-effects residual analysis in which both events and stations are taken as random effects; this breaks the within-event variability, ϕ, into two components: ϕ_{S2S} and ϕ_{SS}. We found that ϕ_{S2S} and ϕ_{SS} were similar for most periods, with an amplitude of about 0.43. The combination of both components gave a ϕ very similar to that used on our GMPM. The residual plots and the bias were also very similar to those for our GMPM, except for the plot of within-event residuals versus V_{S30}, which showed less variability and almost zero bin averages; this is expected as a result of including the station as a random variable. We do not include more specific results in this article, for two reasons: (1) the majority of stations had fewer than five recordings, so the robustness of the results might be questioned, and (2) a detailed study would need to be made of the size of the between-site residuals with what is known, at each site, to be sure that the results make sense. This is beyond the scope of this study.

The BSSA14 between-event variability τ depends only on **M**, as given by equation (10), with the values of $\mathbf{M}_{\tau 1}$ and $\mathbf{M}_{\tau 2}$ being 4.5 and 5.5, respectively. The values of τ_1 and τ_2 in the BSSA14 GMPM were determined from means of the between-event residuals for different magnitude ranges. To develop the τ model (equation 10) for the Greek GMPM, we also computed the means of the between-event residuals for a number of magnitude bins, as shown in Figure 12, for a suite of periods. Based on this figure, we decided that τ would
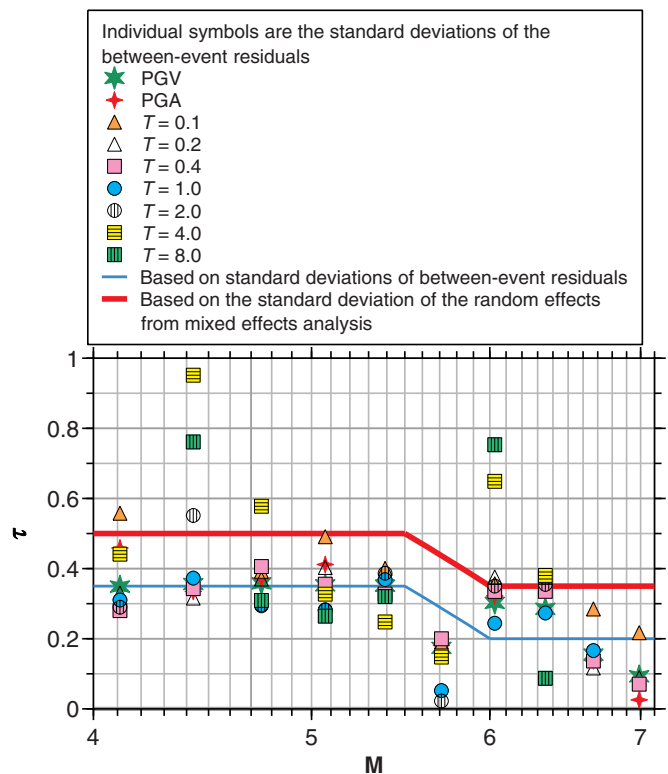
be period independent, with $\mathbf{M}_{\tau 1}$ and $\mathbf{M}_{\tau 2}$ equal to 5.5 and 6.0, respectively (as shown by the lower, thin line in the figure). The values of τ_1 and τ_2 were tentatively chosen to be 0.35 and 0.2, as shown in the figure. To provide a more quantitative estimate of τ_1 and τ_2, we then ran a residual analysis with several ranges of magnitude, with results shown in Figure 13. In comparing Figures 12 and 13, we noticed that the standard deviations of the between-event residuals were less than the mixed-effects estimate of τ for similar magnitude ranges. This occurs because mixed-effects analyses intrinsically account for the error of the event terms in the dispersion computation, which increases the standard deviation. Because the number of recordings per event is relatively small in the Greek dataset (average of 11; in BSSA14 the average is 48), the mixed effects τ is appreciably larger than the standard deviation of the event terms. If epistemic uncertainty in τ is considered in the logic tree applied in hazard analysis, the standard deviation of event terms is preferred for the τ model. If this is not the case, which is likely more common in practice, we recommend using the mixed-effects (higher) value of τ. On this basis, we chose
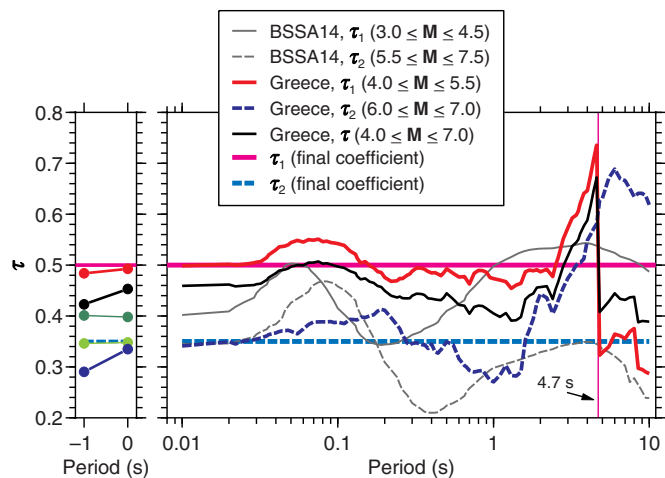
Figure 13. The between-event aleatory variability as a function of period. The τ values for Greece came from the mixed-effects analysis for three magnitude ranges, as shown. The τ values for BSSA14 are based on the standard deviation of between-event residuals in various magnitude bins; those standard deviations can be less than the τ values from mixed-effects analysis, as shown by comparing the previous figure with this one. The color version of this figure is available only in the electronic edition.

Figure 14. Aleatory variability for our final GMPM for $\mathbf{M} \geq 6.0$. The color version of this figure is available only in the electronic edition.

period-independent τ_1 and τ_2 values of 0.5 and 0.35, respectively, as shown in Figure 13. We retained the hinge magnitudes of 5.5 and 6.0 estimated from Figure 12, such that our final τ model is given by the upper, thick line in Figure 12.

To complete the specification of the aleatory variability, Figure 14 shows the total variability σ for $\mathbf{M} \geq 6.0$, as given by equation (9), along with its components ϕ and τ.

Model residuals

A mixed-effects analysis was performed using the final Greek GMPM, to compute partitioned residuals. We show the results for $T = 0.2$ s in Figure 15, which should be compared with Figure 5. A set of residual plots for all GMIMs is included in the supplemental materials. Recalling that the unmodified BSSA14 GMPM was used to produce Figure 5, it is clear that the revised coefficients remove the obvious trends of residuals versus magnitude and distance seen in Figure 5. The bias in the V_{S30} dependence of the within-event residuals remains for small values of V_{S30}, but, as explained before, we made no attempt to remove this bias, because the residuals come from only a few stations.

COMPARISONS TO BSSA14 GMPM AND OTHER GREEK GMPMS

We first compare GMIMs from the GMPM proposed in this article for Greece with those from BSSA14. Plots of median GMIMs versus distance and period are given in Figures 16 and 17, respectively. Our GMIM predictions are shown both when the bias B is added and not added to the fault-type
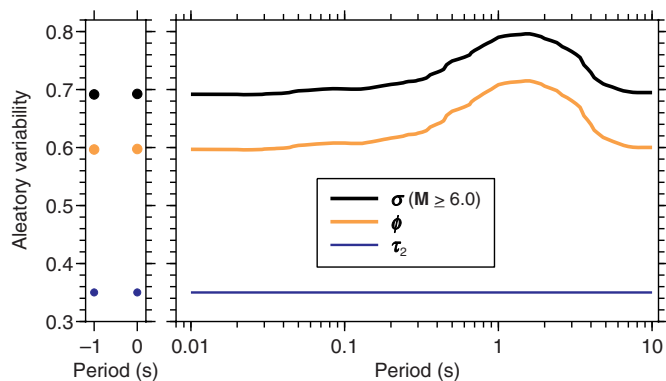
coefficient (in this case e_1, as we are only considering strike-slip events). To remind the reader, adding B will reduce the predicted motions and make them more consistent with the recorded motions used to derive the Greek GMPM. On the other hand, not adding B to the fault-type coefficient should make the predicted median amplitudes for $\mathbf{M} > \mathbf{M}_h$ events more similar to those from BSSA14 (notwithstanding the revisions in the distance attenuation and the magnitude scaling).

Examination of Figures 16 and 17 shows patterns generally reflecting these expectations. In general, for periods between about 0.2 and 2.0 s there is relatively good agreement between the GMIMs predicted from the Greek and the BSSA14 GMPM. The most obvious differences between the predicted GMIMs are (1) the greater attenuation with distance for the Greek GMPM for periods less than about 1.0 s, (2) the large differences at periods less than about 0.2 s for $\mathbf{M}$ 5.5, and (3) the increasing difference with period of the Greek GMIMs with and without a bias adjustment, especially for periods greater than 2.0 s. The attenuation difference is the result of the revision to the anelastic attenuation coefficient c_3. The difference in the GMIMs for $\mathbf{M}$ 5.5 is due to a combination of the reduced magnitude scaling for the Greek GMPM (see e_4 in Fig. 7) and the increase of $\mathbf{M}_h$ (Fig. 7), and the dependence of the Greek GMIMs on the bias, which is expected from Figure 8, where the bias trends to more negative values for periods greater than 2.0 s. Recall that studies of individual mid-magnitude Mediterranean events (6.1–6.5) suggest that matching BSSA14 is not desirable, because it overpredicts some GMIMs (Margaris *et al.*, 2010; Stewart *et al.*, 2012; Zimmaro *et al.*, 2018). Applying the bias for the Greek GMPM causes median GMIMs to fall below BSSA14 for $\mathbf{M}$ 5.5 and 6.5 events, and to approximately equal BSSA14 for $\mathbf{M}$ 4.5 events. The evidence from the mid-magnitude events is admittedly anecdotal, so there is room for alternative interpretations of whether to apply the bias or not in forward analysis. We recommend that seismic hazard analyses consider alternate
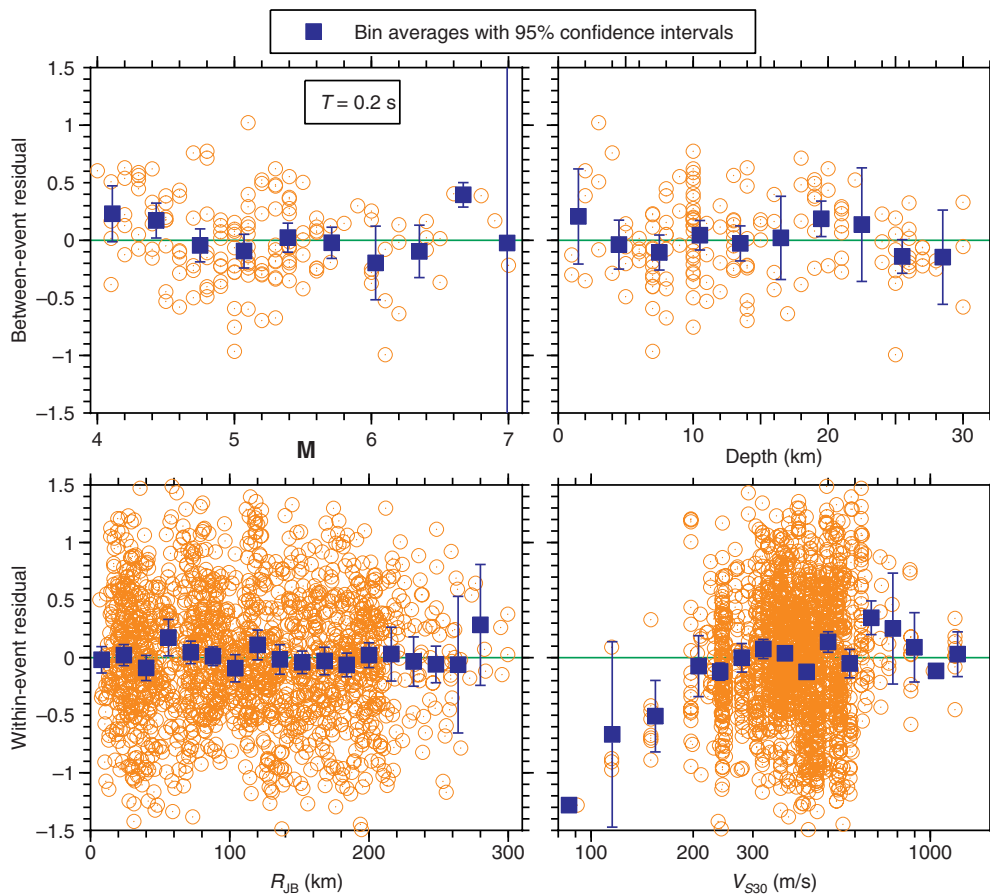
Figure 15. Between-event and within-event residuals (open circles) from the mixed-effects analysis, plotted against key metadata, for a period of 0.2 s. The predicted values used to compute the total residuals (equation 11) came from the coefficients for the Greek GMPM proposed in this article. The color version of this figure is available only in the electronic edition.

GMIMs correspond to geometric means (GM). According to figure 7 in Boore and Kishida (2017), the ratio GM/RotD50 should be less than unity, but no smaller than 0.9 (for $T = 10$ s). Other possible treatments of horizontal components could be vector addition or choosing the largest motion from the two horizontal recordings. According to figures 2 and 6 in Boore and Kishida (2017), these other treatments will be larger than RotD50, but by no more than a factor of 1.29 (for RotD100/RotD50 at $T = 10$ s; we assume that RotD100 is similar to the GMIM obtained by vector addition). These differences in how the horizontal components are used are not enough to account for most of the variations seen in Figures 18 and 19.

The comparisons with PGV and PGA are given in Figure 18. The comparisons are generally better at close distances, but it is interesting and perplexing to see that the two most recent studies—ours and Chousianitis et al. (2018)—

logic-tree branches regarding bias corrections. The effects of the bias are greatly diminished at 1.0 s, but they re-appear at long periods. Because of the limited data, our confidence in the long-period results is lower than that at short periods.

Comparison of GMIMs from earlier Greek-only GMPMs are shown in Figures 18 and 19. We have chosen not to include comparisons with other GMPMs based on Pan-European data, as those models used relatively few Greek data, with a majority of the data coming from Italy. For example, a recent unpublished study by the first author found 179 normal-slip records from Greece in the Engineering Strong-Motion flatfile (Lanzano et al., 2019) from magnitude greater than 4.0 earthquakes, with at least two records within 300 km (and 1696 records from Italy) and 506 records for the same selection criteria in the flatfile used in this article. In comparing the Greek GMIMs, it should be kept in mind that the way in which the data from the two horizontal components have been used might introduce some variation. Of the three earlier studies with Greek-only GMPMs, only Chousianitis et al. (2018) specify how the two horizontal components have been used in the GMPMs; in their case, the

span the range of predicted GMIMs for a given distance, magnitude, or period, with our added-B predictions being low and the Chousianitis et al. (2018) predictions being high. Our PGV and PGA predictions are generally similar to the predictions of Danciu and Tselentis (2007) at close distances, with an increasing divergence at distances greater than about 10 km. The PGA predictions of Skarlatoudis et al. (2003) also agree with ours at close distances and diverge at greater distances, but the PGV predictions of Skarlatoudis et al. (2007) are close to our predictions for most distances.

The comparisons with PSA are shown in Figure 19. Only comparisons with Danciu and Tselentis (2007) are shown, as Chousianitis et al. (2018) do not provide equations for PSA. There are obviously major differences in our predicted PSAs and those of Danciu and Tselentis (2007). Further investigation of the differences just described would require access to the specific databases used in the earlier studies, but this is beyond the scope of this study. Besides, given the larger number of data used in our study, it is perhaps not surprising that differences exist.
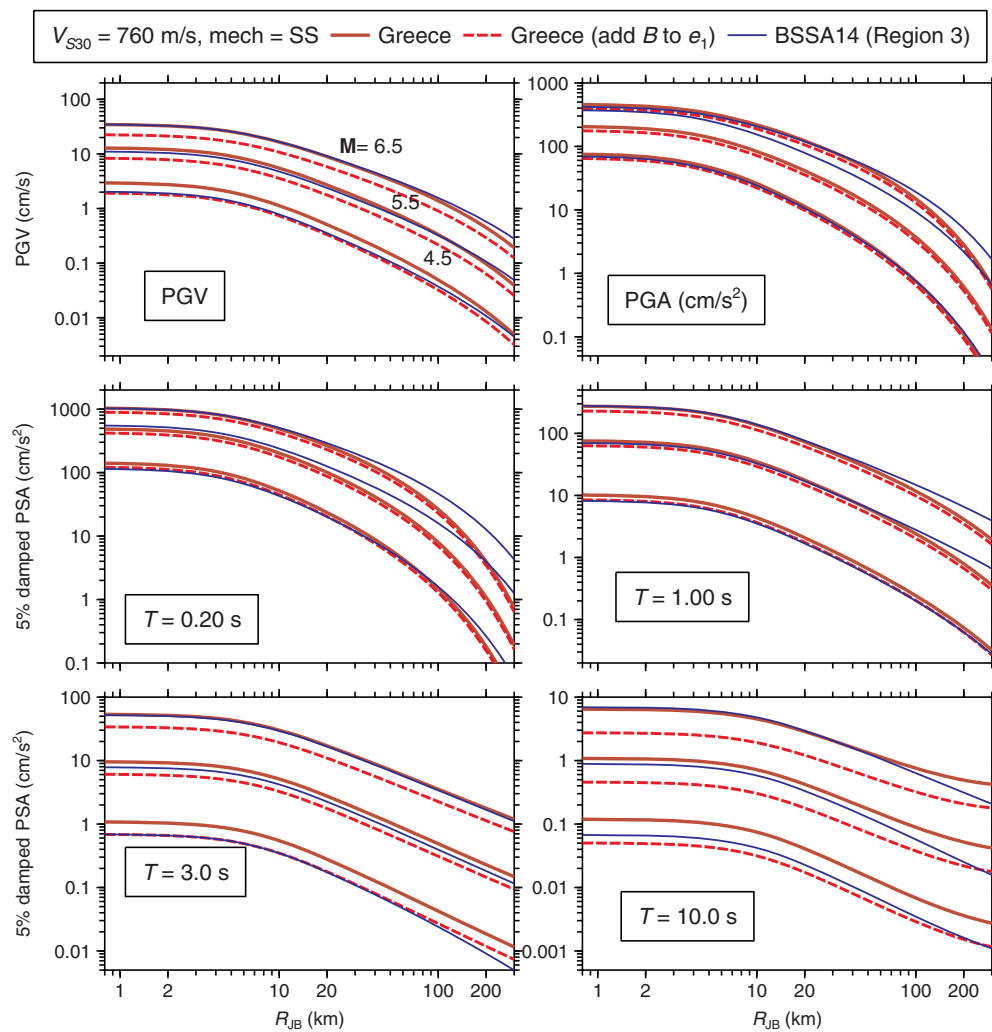
Figure 16. Ground-motion intensity measures (GMIMs) as a function of distance, for a selection of periods. The measures from the GMPM in this article are shown without and with the bias added to the fault-type coefficient (e_1 for this figure, which shows GMIMs for a strike-slip fault type). The color version of this figure is available only in the electronic edition.

BSSA14 GMPM in computing the residuals. We found that most of the BSSA14 coefficients could be used as is. The most important exception was to the anelastic coefficient c_3, which was modified to account for the more rapid attenuation than predicted in the BSSA14 GMPM, even for the region in that GMPM with the most rapid attenuation (Region 3 for Italy and Japan). The next most important modification was to the magnitude scaling, with weaker scaling than in BSSA14 for small magnitudes. Although the limited data from Greece suggest stronger large-magnitude scaling for some GMIMs, we retained the BSSA14 values, which are well constrained from global data. The BSSA14 site amplification model is only modified in a minor way, the linear scaling with V_{S30} being truncated below 200 m/s.

A significant finding was a large negative bias in the residuals, implying smaller recorded ground motions for Greece than in the global dataset used in deriving the BSSA14 GMPM. This finding is not surprising, as similar results have been obtained in prior studies of individual mid-magnitude events in the Mediterranean region (Margaris *et al.*, 2010; Stewart *et al.*, 2012; Zimmaro *et al.*, 2018) and intraslab subduction earthquakes (Skarlatoudis, 2017). We have no definitive explanation for the bias, but available evidence suggests that it is some combination of a regional effect that should be captured in the GMPM and SSI effects that should not. We provide the bias and the fault-type coefficients separately, so that GMIM predictions can be made with or without the bias, to capture this source of epistemic uncertainty in hazard analyses. Adding the bias to the fault-type coefficients results in lower predicted motions.

We recommend the following limits for the predictor variables used in our GMPM:

- magnitude: **M** 4.0–8.0,
- depth: less than or equal to 30 km,

SUMMARY AND DISCUSSION

Using ground-motion data recorded in Greece, available in a recent database (B. Margaris *et al.*, unpublished manuscript, 2021, see Data and Resources), we modified a global GMPM derived from recordings of shallow earthquakes in active crustal regions for application in Greece. The parameter ranges across which the GMPEs in the modified GMPM are calibrated are magnitudes from 4.0 to 7.0, distances from 0 to 300 km, and V_{S30} from 150 to 1200 m/s. However, because the underlying global model is constrained to **M** 8.0, and those features of the model were preserved in the regional model development, we consider the range of applicability for the model to extend to **M** 8.0.

The Greek GMPM produced in this study predicts PGV, PGA, and PSA from periods of 0.01 to 10 s. We based our model on a mixed-effects residual analysis, using the

- R_{JB} distance: 0–300 km,
- V_{S30}: 150–1200 m/s, and
- includes both mainshocks and aftershocks.

These limits are subjective estimates based on the distributions of the recordings in Greece used to develop the equations, as well as the data used to derive the BSSA14 GMPM. The upper magnitude limit for normal-slip earthquakes in BSSA14 is 7.0, but, for the GMPM derived in this article we assume the same upper magnitude limit for all fault types. This assumption was informed by the subjective observation from figure 6 in BSSA14 and Figure 9 in this article that the magnitude scaling observed both in BSSA14 and in this article seems relatively independent of fault type.

The GMPM in this article is for ergodic applications, in which the within-event variability is not dependent on the characteristics of a given site. As a first assessment of a partially or fully nonergodic model, we did a mixed-effects residual analysis in which both events and stations are taken as random effects. We found that the within-station and between-station aleatory variability were about the same, and that the combination gave a within-event variability similar to our ergodic model. For reasons discussed in the section describing the aleatory variability model, we chose not extend to our model to a partially or fully nonergodic model. This would be a useful thing to do in the future, however, particularly after more data are collected (as of now, the majority of the stations have fewer than five recordings).
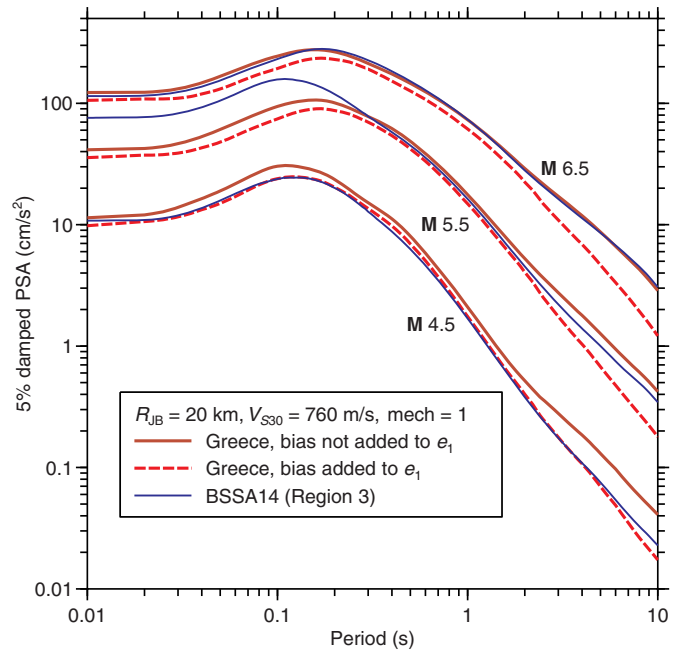

Figure 17. 5% damped pseudospectral acceleration (PSA) as a function of period, for a selection of magnitudes. The measures from the GMPM in this article are shown without and with the bias added to the fault-type coefficient (e_1 for this figure, which shows PSAs for a strike-slip fault type). For comparison, the PSAs for the BSSA14 GMPM are also shown. The color version of this figure is available only in the electronic edition.
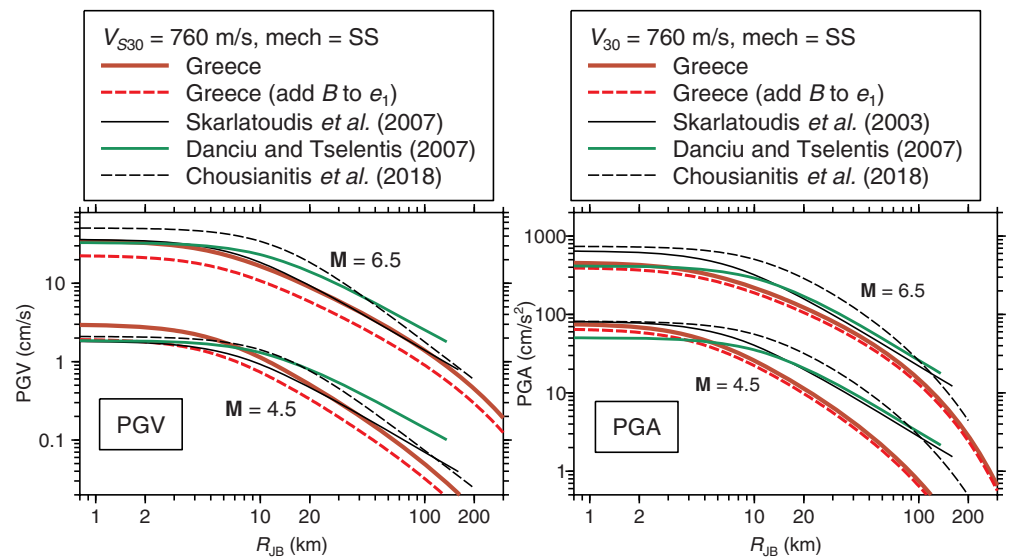
DATA AND RESOURCES

The ground-motion database used in this article is described by B. Margaris *et al.* (unpublished manuscript, 2021, see Data and Resources) and is available as a supplemental material to that article. Most of the analysis used scripts written in R (R Core Team, A language and environment for statistical computing. R Foundation for Statistical Computing, Vienna, Austria, available at https://www.R-project.org/), relying heavily on the mixed-effects analysis provided by the function lme in the nlme package (J. Pinheiro, D. Bates, S. DebRoy, D. Sarkar, and R Core Team, 2020, nlme: Linear and Nonlinear Mixed Effects Models, R package version 3.1-148, available at https://CRAN.R-project.org/package=nlme). The figures were prepared using CoPlot (www.cohort.com). The search for previous ground-motion prediction

Figure 18. GMIMs as a function of distance, for PGV and PGA. This figure compares the GMIMs from the Greek GMPM proposed in this article with those from three earlier publications. For clarity, only results for magnitudes 4.5 and 6.5 are shown. The measures from the GMPM in this article are shown without and with the bias added to the fault-type coefficient (e_1 for this figure, which shows GMIMs for a strike-slip fault type). The color version of this figure is available only in the electronic edition.
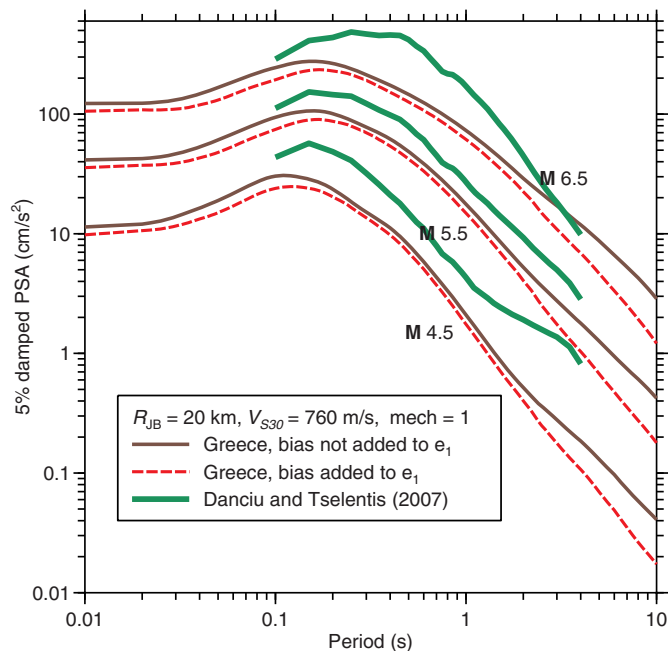
Figure 19. 5% damped PSA as a function of period, for a selection of magnitudes. This is similar to Figure 17, except the GMIMs for BSSA14 have been replaced with those from the Danciu and Tselentis (2007) GMPM. Results for Chousianitis et al. (2018) are not shown, as they did not provide equations for PSA. The color version of this figure is available only in the electronic edition.

models (GMPMs) for Greece was greatly aided by John Douglas's compendium of GMPMs (ground-motion prediction equations 1964–2019, available at http://www.gmpe.org.uk/). All websites were last accessed in November 2020. The other relevant data are from the unpublished manuscript by B. Margaris, E. M. Scordilis, J. P. Stewart, D. M. Boore, N. Theodulidis, I. Kalogeras, N. Melis, A. Skarlatoudis, N. Klimis, and E. Seyhan, 2021, Hellenic strong-motion database with uniformly assigned source and site metadata for period of 1972–2015, submitted to *Seismol. Res. Lett.* The supplemental material includes a cover letter describing four files also provided in the supplemental material: a csv file of the coefficients in the equations comprising the proposed GMPM for Greece, a pdf file of the residual plots (similar to Fig. 15), a pdf file of plots of within-event residuals versus distance for three magnitude bins, for all 107 ground-motion intensity measures (GMIMs), and a zip file containing four csv files that are the output of the residual analysis; these zip files contain a wealth of information, including the metadata and GMIMs used in the analysis, as well as much material from the output of the mixed-effects analysis.

ACKNOWLEDGMENTS

REFERENCES

Akkar, S., M. A. Sandıkkaya, and J. J. Bommer (2014). Empirical ground-motion models for point-and extended-source crustal earthquake scenarios in Europe and the Middle East, *Bull. Earthq. Eng.* **12,** 359–387.

Akkar, S., M. A. Sandıkkaya, M. Şenyurt, A. A. Sisi, B.Ö. Ay, P. Traversa, J. Douglas, F. Cotton, L. Luzi, B. Hernandez, and S. Godey (2014). Reference database for seismic ground-motion in Europe (RESORCE), *Bull. Earthq. Eng.* **12,** 311–339.

Al Atik, L., N. Abrahamson, J. J. Bommer, F. Scherbaum, F. Cotton, and N. Kuehn (2010). The variability of ground-motion prediction models and its components, *Seismol. Res. Lett.* **81,** 794–801.

Bindi, D., S. R. Kotha, G. Weatherill, G. Lanzano, L. Luzi, and F. Cotton (2019). The pan-European engineering strong motion (ESM) flatfile: Consistency check via residual analysis, *Bull. Earthq. Eng.* **17,** 583–602.

Bindi, D., M. Massa, L. Luzi, G. Ameri, F. Pacor, R. Puglia, and P. Augliera (2014). Pan-European ground-motion prediction equations for the average horizontal component of PGA, PGV, and 5%-damped PSA at spectral periods up to 3.0 s using the RESORCE dataset, *Bull. Earthq. Eng.* **12,** 391–430.

Bommer, J. J., and J. E. Alarcon (2006). The prediction and use of peak ground velocity, *J. Earthq. Eng.* **10,** 1–31.

Boore, D. M. (2010). Orientation-independent, nongeometric-mean measures of seismic intensity from two horizontal components of motion, *Bull. Seismol. Soc. Am.* **100,** 1830–1835.

Boore, D. M. (2020). Revision of Boore (2018) ground-motion predictions for central and eastern North America: Path and offset adjustments and extension to 200 m/s ≤ V_{S30} ≤ 3000 m/s, *Seismol. Res. Lett.* **91,** 977–991.

Boore, D. M., and G. M. Atkinson (2008). Ground-motion prediction equations for the average horizontal component of PGA, PGV, and 5%-damped PSA at spectral periods between 0.01 s and 10.0 s, *Earthq. Spectra* **24,** 99–138.

Boore, D. M., and T. Kishida (2017). Relations between some horizontal-component ground-motion intensity measures used in practice, *Bull. Seismol. Soc. Am.* **107,** 334–343.

Boore, D. M., A. Skarlatoudis, B. Margaris, C. Papazachos, and C. Ventouzi (2009). Along-arc and back-arc attenuation, site response, and source spectrum for the intermediate-depth January 8, 2006, M 6.7 Kythera, Greece, earthquake, *Bull. Seismol. Soc. Am.* **99,** 2410–2434.

Boore, D. M., J. P. Stewart, E. Seyhan, and G. M. Atkinson (2013). NGA-West 2 equations for predicting response spectral accelerations for shallow crustal Earthquakes, *PEER 2013/05*, Pacific Earthquake Engineering Research Center, Berkeley, California, 135 pp.

Boore, D. M., J. P. Stewart, E. Seyhan, and G. M. Atkinson (2014). NGA-West 2 equations for predicting PGA, PGV, and 5%-damped PSA for shallow crustal earthquakes, *Earthq. Spectra* **30,** 1057–1085.

Booth, E. (2007). The estimation of peak ground-motion parameters from spectral ordinates, *J. Earthq. Eng.* **11,** 13–32.

Bozorgnia, Y., N. A. Abrahamson, L. Al Atik, T. D. Ancheta, G. M. Atkinson, J. W. Baker, A. Baltay, D. M. Boore, K. W. Campbell, B. S.-J. Chiou, et al. (2014). NGA-West2 research project, Earthq. Spectra 30, 973–987.

Bradley, B. A. (2013). A New Zealand-specific pseudospectral acceleration ground-motion prediction equation for active shallow crustal earthquakes based on foreign models, Bull. Seismol. Soc. Am. 103, 1801–1822.

Chiou, B. S.-J., and R. R. Youngs (2008). NGA model for average horizontal component of peak ground motion and response spectra, PEER Report 2008/09, Pacific Earthquake Engineering Research Center, Berkeley, California.

Chousianitis, K., V. Del Gaudio, P. Pierri, and G.-A. Tselentis (2018). Regional ground-motion prediction equations for amplitude-, frequency response-, and duration-based parameters for Greece, Earthq. Eng. Struct. Dynam. 47, 2252–2274.

Conti, R., M. Morigi, E. Rovithis, N. Theodoulidis, and C. Karakostas (2018). Filtering action of embedded massive foundations: New analytical expressions and evidence from 2 instrumented buildings, Earthq. Eng. Struct. Dynam. 47, 1229–1249.

Contreras, V., J. P. Stewart, T. Kishida, R. B. Darragh, B. S. J. Chiou, S. Mazzoni, N. Kuehn, S. K. Ahdi, K. Wooddell, R. R. Youngs, et al. (2020). Source and path metadata, chapter 4 in data resources for NGA-subduction project, in J. P. Stewart (Editor), PEER Report 2020/02, Pacific Earthquake Engineering Research Center, UC Berkeley.

Danciu, L., and G.-A. Tselentis (2007). Engineering ground-motion parameters attenuation relationships for Greece, Bull. Seismol. Soc. Am. 97, 162–183.

Gülerce, Z., B. Kargıoğlu, and N. A. Abrahamson (2016). Turkey-adjusted NGA-W1 horizontal ground motion prediction models, Earthq. Spectra 32, 75–100.

Hatzidimitriou, P., C. Papazachos, A. Kiratzi, and N. Theodulidis (1993). Estimation of attenuation structure and local earthquake magnitude based on acceleration records in Greece, Tectonophysics 217, 243–253.

Kotha, S. R., D. Bindi, and F. Cotton (2016). Partially non-ergodic region specific GMPE for Europe and Middle-East, Bull. Earthq. Eng. 14, 1245–1263.

Kotha, S. R., G. Weatherill, D. Bindi, and F. Cotton (2020). A regionally-adaptable ground-motion model for shallow crustal earthquakes in Europe, Bull. Earthq. Eng. 18, 4091–4125.

Kuehn, N. M., and F. Scherbaum (2016). A partially non-ergodic ground-motion prediction equation for Europe and the Middle East, Bull. Earthq. Eng. 14, 2629–2642.

Lanzano, G., S. Sgobba, L. Luzi, R. Puglia, F. Pacor, C. Felicetta, M. D'Amico, F. Cotton, and D. Bindi (2019). The pan-European Engineering Strong Motion (ESM) flatfile: Compilation criteria and data statistics, Bull. Earthq. Eng. 17, 561–582.

Margaris, B., G. Athanasopoulos, G. Mylonakis, C. Papaioannou, N. Klimis, N. Theodulidis, A. Savvaidis, V. Efthymiadou, and J. P. Stewart (2010). The 8 June 2008 M_w 6.4 Achaia–Elia, Greece earthquake: Source characteristics, ground motions, and ground failure, Earthq. Spectra 26, 399–424.

National Institute of Standards and Technology (NIST) (2012). Soil-structure interaction for building structures, Report No. NIST GCR 12-917-21, National Institute of Standards and Technology, U.S. Department of Commerce, Washington, D.C.

Scasserra, G., J. P. Stewart, P. Bazzurro, G. Lanzo, and F. Mollaioli (2009). A comparison of NGA ground-motion prediction equations to Italian data, Bull. Seismol. Soc. Am. 99, 2961–2978.

Seyhan, E., and J. P. Stewart (2014). Semi-empirical nonlinear site amplification from NGA-West2 data and simulations, Earthq. Spectra 30, 1241–1256.

Skarlatoudis, A. A. (2017). Applicability of ground-motion prediction equations to a Greek within-slab earthquake dataset, Bull. Earthq. Eng. 15, 3987–4008.

Skarlatoudis, A. A., C. B. Papazachos, B. N. Margaris, N. Theodulidis, Ch. Papaioannou, I. Kalogeras, E. M. Scordilis, and V. Karakostas (2003). Empirical peak ground-motion predictive relations for shallow earthquakes in Greece, Bull. Seismol. Soc. Am. 93, 2591–2603.

Skarlatoudis, A. A., C. B. Papazachos, B. N. Margaris, N. Theodulidis, Ch. Papaioannou, I. Kalogeras, E. M. Scordilis, and V. Karakostas (2007). Erratum to empirical peak ground-motion predictive relations for shallow earthquakes in Greece, Bull. Seismol. Soc. Am. 97, 2219–2221.

Skarlatoudis, A. A., C. B. Papazachos, B. N. Margaris, C. Ventouzi, I. Kalogeras, and the EGELADOS Group (2013). Ground-motion prediction equations of intermediate-depth earthquakes in the Hellenic Arc, Southern Aegean Subduction area, Bull. Seismol. Soc. Am. 103, 1952–1968.

Sotiriadis, D., N. Klimis, B. Margaris, and A. Sextos (2019). Influence of structure–foundation–soil interaction on ground motions recorded within buildings, Bull. Earthq. Eng. 17, 5867–5895.

Sotiriadis, D., N. Klimis, B. Margaris, and A. Sextos (2020). Analytical expressions relating free-field and foundation ground motions in buildings with basement, considering soil-structure interaction, Eng. Struct. 216, 110757.

Stewart, J. P., G. Lanzo, A. Pagliaroli, G. Scasserra, G. DiCapua, S. Peppolini, R. Darragh, and N. Gregor (2012). Ground motion recordings from the M_w 6.3 2009 L'Aquila earthquake in Italy and their engineering implications, Earthq. Spectra 28, 317–345.

Stewart, J. P., G. A. Parker, G. M. Atkinson, D. M. Boore, Y. M. Hashash, and W. J. Silva (2020). Ergodic site amplification model for central and eastern North America, Earthq. Spectra 36, 1–12.

Zimmaro, P., G. Scasserra, J. P. Stewart, T. Kishida, G. Tropeano, M. Castiglia, and P. Pelekis (2018). Strong ground motion characteristics from 2016 central Italy earthquake sequence, Earthq. Spectra 34, 1611–1637.